Journal of Materials Chemistry A

ROYAL SOCIETY OF CHEMISTRY

PAPER

View Article Online
View Journal | View Issue

Cite this: J. Mater. Chem. A, 2026, 14, 19694

Cyclic voltammetry driven Bi–Ag single-atom alloy electrocatalysts for enhanced CO_2-to-formate conversion

Yongsu An, [a] Sunglun Kwon,[b] Young Heon Kim, [c] Chan Woo Lee [d]* and Duk-Young Jung [a]*

Single-atom alloy (SAA) catalysts offer synergistic electronic interactions, optimized adsorption environments, and maximized atomic utilization. Here, we report an electrochemical strategy to synthesize Bi single atoms dispersed on Ag (Bi–Ag SAAs), which serve as a promising catalyst platform for CO_2-to-formate conversion. HAADF-STEM/EDS, XPS, and XRD collectively demonstrate that cyclic voltammetry treatment reconstructs a thermally evaporated Bi layer on Ag nanoparticles supported on a carbon electrode into atomically dispersed Bi sites on Ag. The resulting Bi–Ag SAAs catalyst derived from a 15 nm Bi layer exhibited 1.9-fold higher formate faradaic efficiency and 3.5-fold higher formate selectivity than non-CV-treated samples, despite a substantially lower Bi loading. Electrochemical impedance spectroscopy reveals a charge-transfer-resistance hierarchy of Bi > AgBi > CV-AgBi under both N_2 and CO_2 saturated conditions, indicating enhanced interfacial charge transfer for CO_2 reduction at atomically dispersed Bi sites. This work provides key insight into how CV-driven reconstruction can be leveraged to create atomically dispersed single-atom alloys for advanced CO_2-reduction catalyst design.

Received 13th January 2026
Accepted 9th April 2026

DOI: 10.1039/d6ta00340k

rsc.li/materials-a

1. Introduction

The alarming rise in atmospheric carbon dioxide (CO_2) levels has emerged as one of the most critical contributors to global warming. In response, the electrochemical CO_2 reduction reaction (CO_2RR) has attracted growing interest as a promising route to not only mitigate CO_2 emissions but also convert it into value-added chemicals such as methanol, ethanol, and formic acid.[1–3] Among these, formic acid stands out due to its high volumetric hydrogen content, non-toxicity, and capability to release hydrogen under ambient conditions, making it a potential candidate for hydrogen storage applications.[4–7] In pursuit of selective CO_2-to-formate conversion, p-block metals such as Bi, Sn, and In have demonstrated excellent catalytic activity,[8,9] especially Bi exhibits the highest selectivity and lowest cost among them.[10–14] While monometallic Bi catalysts show high performance for formate production, recent studies suggest that heterometallic systems can offer additional advantages such as synergistic electronic interactions, optimized adsorption sites, and enhanced atomic utilization.[15–20] Our previous work[21] on the micro Bi–nano Ni hierarchical system demonstrated that while full wetting significantly enhanced formate production by increasing the surface area, hydrogen evolution reactions are not completely suppressed due to the bulk-like characteristics of the Ni nanoparticles. On the other hand, single-atom alloys (SAAs) are free from such concerns, enabling the precise tailoring of reaction pathways toward the target product.

Despite extensive research on SAAs, reports on Bi-based catalysts remain scarcely explored,[14,22–27] with only a few reports on Bi SAAs involving Fe,[25] Pd,[26] and SnO_2.[27] This lack of studies is primarily attributed to the synthetic challenges associated with incorporating Bi as a single atom. Bi metal adopts a rhombohedral lattice ($a = 0.454$ nm), which is distinct from the crystal structures of most other metals and typically exhibits lattice mismatches exceeding 10%. This structural mismatch can promote the formation of Janus-type architectures during wet-chemical synthesis, hindering uniform Bi atom dispersion over the core surface and complicating SAAs fabrication.[28–30] Lattice mismatch alone cannot account for the synthetic challenges of Bi SAAs. Instead, surface and interfacial energies, cohesive and segregation energetics, and growth kinetics—including precursor injection and reduction rates—collectively determine whether Bi atoms remain as dispersed single atoms or phase-separate into Janus-type architectures.[16,31–34] Given the interplay of these multiple variables, the synthesis of Bi SAAs demands a highly refined and

[a]Department of Chemistry, Sungkyun Advanced Institute of Nanotechnology (SAINT), Sungkyunkwan University, Suwon, 16419, Republic of Korea. E-mail: dyjung@skku.edu

[b]Department of Chemistry, The Catholic University of Korea, Bucheon, 14662, Republic of Korea

[c]Graduate School of Analytical Science and Technology (GRAST), Chungnam National University, Daejeon, 34134, Republic of Korea

[d]Department of Chemistry, Kookmin University, Seoul, 02707, Republic of Korea

precisely controlled process to achieve the desired atomic configuration.

Notably, another fundamental limitation is the intrinsic oxophilicity of Bi. Even ultrathin Bi coatings on metallic cores oxidize rapidly to Bi_2O_3 upon brief air exposure.[35] Once oxidized, Bi layers undergo solid-state dewetting and islanding, yielding Bi aggregates rather than thin layers with conformal coverage.[35–38] The pronounced oxophilicity of Bi inherently undermines stable Bi structures unless Bi is directly synthesized as a single atom dispersion and firmly anchored to the metal substrate *via* robust Bi–M metallic bonding. As mentioned above, the synthesis of Bi SAAs is fundamentally hindered by a combination of intrinsic limitations stemming from unique properties of Bi. These physicochemical constraints severely impede synthesis *via* conventional approaches, necessitating the development of new synthetic strategy that can effectively overcome these hurdles to stabilize atomically dispersed Bi SAAs.

In this work, we introduce a voltammetry-regulated strategy that enables the formation of Bi SSAs on Ag nanoparticles through selective redox cycling in chloride electrolytes. By combining thermal evaporation of conformal Bi overlayers with controlled cyclic voltammetry, Bi is selectively oxidized and subsequently reduced onto Ag, producing atomically isolated Bi sites without forming extended Bi domains. Comprehensive structural and electrochemical analyses reveal that this process induces Bi incorporation into the Ag lattice, establishes a thin AgCl/BiOCl passivation that is reductively removed during CO_2RR, and ultimately yields stable Bi–Ag SAA catalytic centers. This synthetic method not only maximizes Bi atom utilization but also enhances formate production and selectivity relative to thick Bi layers, demonstrating the unique reactivity of Bi single-atom sites in CO_2 electroreduction. Accordingly, this work establishes a robust and generalizable electrochemical route for constructing Bi SAAs and elucidates the critical role of selective Bi redox processes in tailoring active sites for CO_2RR.

2. Experiments

2.1. Materials and chemicals

$AgNO_3$ (99.8%), ethylene glycol ($C_2H_6O_2$, 99.9%) and isopropyl alcohol anhydrous (C_3H_8O, 99.9%) were supplied by Samchun Chemicals. Polyvinylpyrrolidone ($M_w \approx 55\,000$) and $NaSH \cdot xH_2O$ were purchased by Sigma-Aldrich. The Nafion NR211 membrane was obtained from Ion Power, Inc., a Nafion solution (5 weight%, DuPont) from NanoHoldings (Korea), and carbon paper (Sigracet 28 BC) from Fuel Cell Store. Bi shot (99.999%) was purchased by ITASCO.

2.2. Sample preparation

Silver nanoparticles were synthesized by a polyol method[39] with minor modifications. Reactions were carried out in a 50 mL round-bottom flask immersed in a silicone-oil bath. Ethylene glycol (EG, 6.0 mL) was heated to 150 °C under stirring (320 rpm), and all reagents were added as rapid, single-shot pipette injections. A solution of $NaSH \cdot 1.5H_2O$ in EG (3.0 mM; 70 μL) was injected, followed by PVP ($M_w \approx 55\,000$) in EG (20 mg mL^{-1}; 1.5 mL). After 8 minutes at 150 °C, $AgNO_3$ in EG (282 mM; 0.50 mL) was injected and the reaction was continued for 20 minutes until the dispersion turned green-ochre, then quenched in an ice bath. The dispersion was diluted with acetone (1 : 4, v/v), divided into two conical tubes, and centrifuged (2000*g*, 25–30 minutes). Pellets were redispersed in deionized water (6 mL), transferred to microcentrifuge tubes, and centrifuged at 8000*g* for 10 minutes with isopropanol (IPA) washing; this step was repeated three times. Purified Ag nanoparticles were finally dispersed in EG (8.0 mL) containing PVP (20 mg mL^{-1}) for subsequent processing.

To remove residual PVP/EG prior to electrode fabrication, 80 μL of the prepared Ag dispersion in EG was diluted in 1.5 mL IPA and centrifuged twice. The Ag was resuspended in IPA containing 10 μL of Nafion solution (5 weight%) and drop-cast onto 1 × 1 cm^2 carbon paper pre-cleaned by O_2 plasma for 5 minutes. This Ag-loaded electrode is hereafter denoted "Ag". Bi was subsequently deposited onto Ag by thermal evaporator (REP-5004, SNTEK, Korea). The deposition was carried out at a chamber pressure of 6×10^{-6} torr and a constant deposition rate of 0.5 Å s^{-1}, with the substrate maintained at an ambient temperature of 20 °C. The nominal thicknesses of 2, 5, 15, 25, 35, and 45 nm, yielding Bi-overcoated Ag electrodes denoted "$AgBi_t$" (t = nominal Bi thickness in nm).

Cyclic voltammetry was performed in N_2-purged 0.1 M HCl using a three-electrode configuration. The AgBi electrodes prepared above were used as the working electrode with an Ag/AgCl (3 M KCl) reference electrode and a graphite rod counter electrode. The potential range was between −0.08 and +0.08 V *vs.* Ag/AgCl at a scan rate of 50 mV s^{-1}. After CV treatment, the electrodes were rinsed several times with anhydrous IPA and dried under vacuum. Samples subjected to cyclic voltammetry in 0.1 M HCl are labeled "CV-$AgBi_t$" (where t is the nominal Bi thickness in nm).

2.3. Characterization

The samples were analyzed by field-emission scanning electron microscopy (FE-SEM, JSM-7100F, JEOL), energy-dispersive spectroscopy (EDS, attachment for SEM, Oxford), X-ray diffraction (XRD, Rigaku SmartLab SE diffractometer) with Cu-Kα radiation (λ = 1.5405 Å), and field-emission gun (FEG) TEM operating at 300 keV (Thermo Fisher Scientific Inc., Spectra 300 TEM) with STEM unit. X-ray photoelectron spectroscopy (XPS) was performed using a concentric hemispherical analyzer (PHOIBOS 150 1D-DLD, SPECS, Germany) with a monochromatic Al Kα source ($h\nu$ = 1486.6 eV). Nuclear magnetic resonance (FT-NMR 500 MHz, Unity Inova, Varian), gas chromatography (GC, 6890N, Agilent) was used to determine the H_2 and CO contents of the electrochemical CO_2 reduction reaction.

2.4. Electrochemical measurements

Chronoamperometry was performed using a PGSTAT128N (Autolab) at −1.5 V (*vs.* Ag/AgCl, 3 M KCl). All electrochemical measurements were carried out in an H-cell with a Nafion NR211 membrane using a 0.5 M $KHCO_3$ solution at room

temperature. Prepared samples were used as the working electrodes, whereas a graphite rod and Ag/AgCl (3 M KCl) served as the counter and reference electrodes, respectively. In addition, CO_2 was bubbled into a 0.5 M $KHCO_3$ solution in the cathode compartment.

Electrochemical impedance spectroscopy (EIS) was performed using a CompactStat spectrometer (Ivium Technologies). The counter and reference electrodes were a graphite rod and Ag/AgCl (3 M KCl), respectively. Bi, AgBi, and CV-AgBi samples measured in 0.5 M $KHCO_3$ electrolyte with N_2 and CO_2 saturated condition. The AC amplitude was 5 mV and the frequency range was from 100 MHz to 0.1 Hz.

3. Results and discussion

The strategy for synthesizing Bi SAAs on Ag nanoparticles is illustrated in Fig. 1a. Ag nanoparticles (~50 nm) were first prepared *via* a conventional solution-based method and deposited onto carbon paper by drop-casting. Subsequently, Bi thin layers were deposited by thermal evaporation to achieve conformal coverage over the Ag surface, which is critical for enabling uniform electrochemical modification during the following CV treatment, performed in 0.1 M HCl to induce the formation of atomically dispersed Bi on the Ag surface (CV-AgBi) (Fig. 1b–e). Silver was selected as the core metal owing to its established CO_2RR activity and broad applicability in bimetallic SAAs systems.[40–42]

SEM images (Fig. S1) reveal the morphologies of Ag nanoparticles and the Bi overlayer as a function of Bi-layer thickness (denoted as $AgBi_{2nm}$, $AgBi_{5nm}$, $AgBi_{15nm}$, $AgBi_{25nm}$, $AgBi_{35nm}$, and $AgBi_{45nm}$), as well as the effect of the CV treatment. The Ag nanoparticle without Bi layer showed essentially unchanged shape, but AgBi samples exhibited edge dissolution by CV. This morphological change arises from the CV-induced redeposition of Bi onto Ag rather than from the direct effect of CV on Ag itself. Furthermore, SEM images taken after 1 hour of the CO_2RR (Fig. S2) show no significant morphological changes compared to the initial state, confirming the structural stability of the CV-$AgBi_{15nm}$ during the early stage of the reaction.

In the CV-$AgBi_{15nm}$ sample, HAADF-STEM and related EDS mapping (Fig. 1b–d) showed only trace Bi localized on Ag, without evidence of extended Bi domains. High-resolution HAADF-STEM image and corresponding EDS (Fig. 1e and S3) further revealed highly dispersed, isolated Bi atoms across the Ag surface. The absence of continuous Bi phases together with the ultra-low Bi signal in elemental maps demonstrated the single-atom nature of the Bi species after CV treatment.

The application of CV rests on two complementary properties (Fig. 2 and S4–S7): (i) the standard reduction potentials of the constituent elements and (ii) the electronic conductivities. These features enabled the selective oxidation of Bi, which was subsequently re-reduced selectively on the Ag surface. Fig. 2 presents the CV responses of bare carbon paper, Ag-deposited carbon paper (Ag), 2 nm-thick Bi deposited on Ag ($AgBi_{2nm}$)

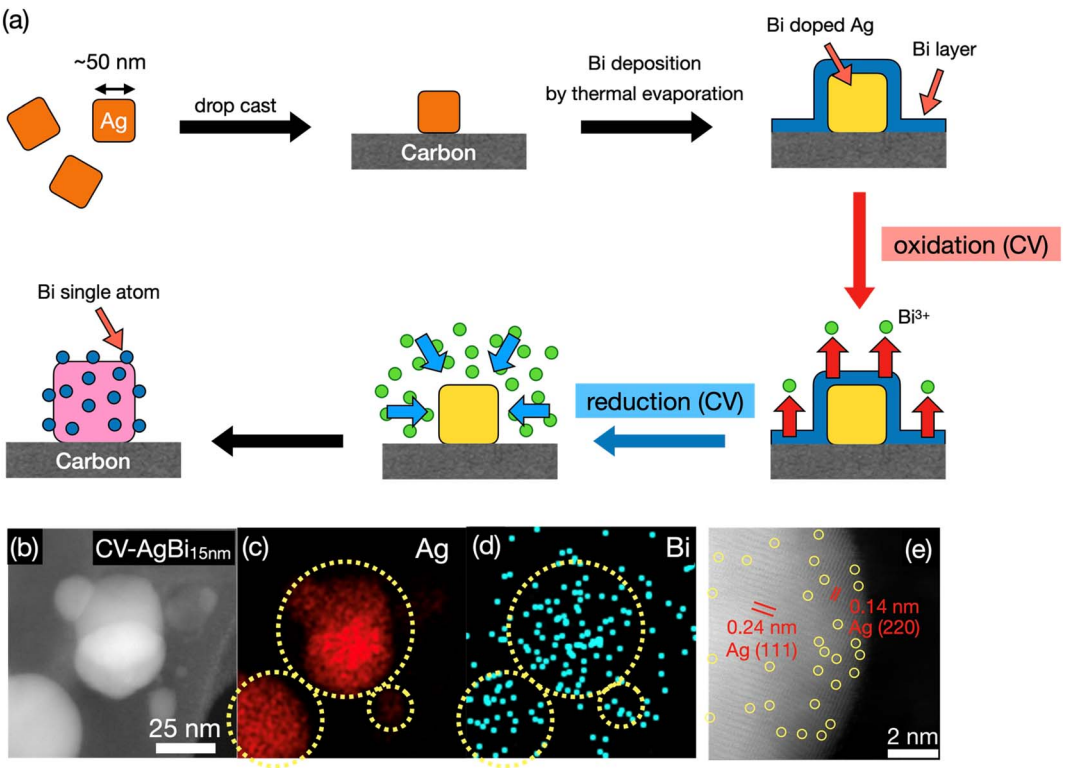

Fig. 1 (a) Schematic illustration of the synthesis of CV-AgBi, Bi deposition followed by cyclic voltammetry (CV) in 0.1 M HCl. (b) HAADF-STEM and related EDS-mapping results of (c) Ag, (d) Bi for CV-$AgBi_{15nm}$. The blue circles in (d) serve as graphical guides to highlight representative Bi single atom sites. (e) High-resolution HAADF-STEM image of CV-$AgBi_{15nm}$.

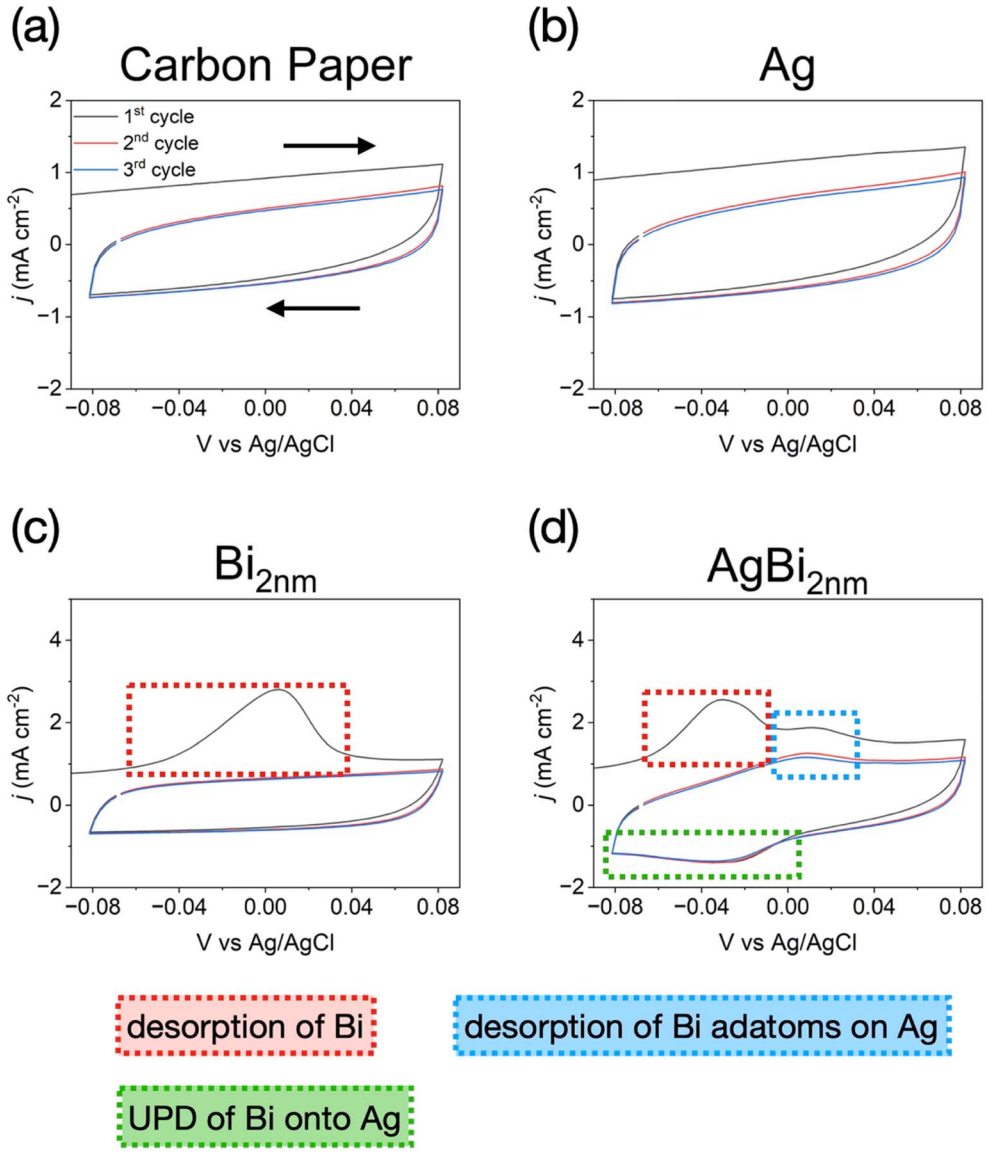

Fig. 2 Cyclic voltammetry curves of (a) carbon paper, (b) Ag, (c) Bi_{2nm} and (d) $AgBi_{2nm}$.

and Ag-free 2 nm-thick Bi-coated carbon paper (Bi_{2nm}), enabling a comparative analysis of electrochemical behavior. Within the potential window of −0.08 to 0.08 V, carbon paper (Fig. 2a) and Ag (Fig. 2b) showed no discernible redox features attributable to silver oxides or silver chloride (Fig. S4c and S6), confirming that Ag remained in the metallic state (Ag^0) within this potential window. By contrast, Bi_{2nm} (Fig. 2c) exhibited a distinct oxidation peak indicated by the red dashed line. Notably, a corresponding reduction feature was absent for Bi_{2nm}, indicating that Bi was not reduced within the applied potential range.

$AgBi_{2nm}$ showed two additional peaks in the CV curves (Fig. 2d), which emerged in the oxidative scan (blue box), following the oxidation of Bi (red box), and the other (green box) during the reductive scan. The oxidation potentials for monolayer Bi are distinct from bulk Bi.[43] The blue box is assigned to the oxidation peak of Bi atoms on the Ag nanoparticle surface. The oxidation of Bi on Ag needs higher energy than that of Bi on carbon. The reduction peak (green box) was observed exclusively in the presence of Ag, suggesting that this process corresponds to the reduction of Bi onto Ag. A comparison of $AgBi_{1nm}$ and Bi_{1nm} in Fig. S4 demonstrated that the required potentials for overpotential deposition (OPD) and underpotential deposition (UPD) are substrate-dependent,[44,45] indicating that the reduction peak in Fig. 2d corresponds to the UPD of Bi on Ag.

Notably, the Bi oxidation peak (red box in Fig. 2d) was observed only during the first CV cycle for the Bi_{2nm} and $AgBi_{2nm}$ samples, whereas the Ag-related peaks (blue box) persisted in the subsequent scans. This behavior is consistent with the formation of BiOCl in the HCl electrolyte, whose reduction occurs at more negative potential than that of free Bi ions (Fig. S5) and peak intensity is proportional to the thickness of Bi layer. Chloride ion in HCl electrolyte scavenges Bi ion to form BiOCl, thereby depleting free Bi ion and suppressing Bi

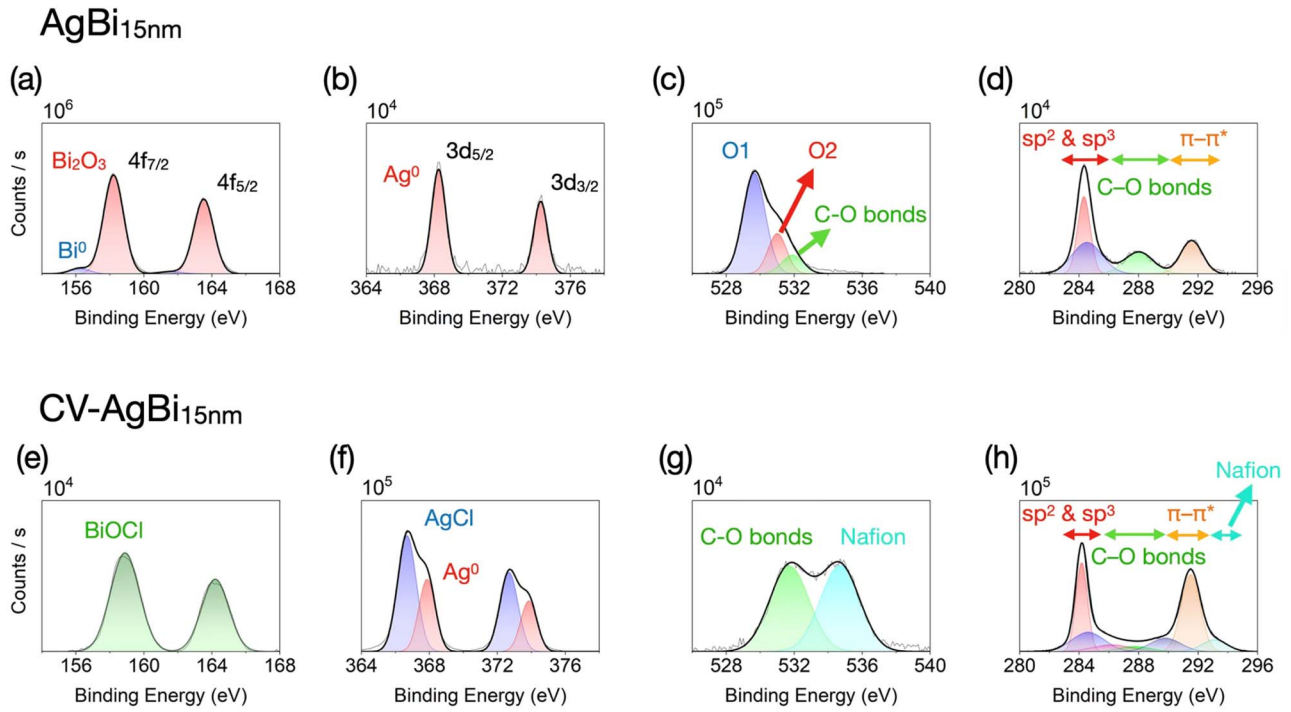

Fig. 3 XPS spectra of $AgBi_{15nm}$ (a–d) and CV-$AgBi_{15nm}$ (e–h). Spectra are shown for (a and e) Bi 4f, (b and f) Ag 3d, (c and g) O 1s, and (d and h) C 1s, respectively.

reduction within the scanned potential window (−0.08 V to 0.08 V). The CV results strongly suggest that Bi was selectively retained on Ag sites, rather than on the carbon substrate, following the initial oxidation scans.

The number of CV cycles required to remove Bi completely from the carbon electrode increases with the thickness of the deposited Bi layer as shown in Fig. S7. For Bi thicknesses of 2 and 5 nm ($AgBi_{2nm}$ and $AgBi_{5nm}$), a single CV cycle is sufficient for complete removal. In contrast, the 15 and 25 nm layers ($AgBi_{15nm}$ and $AgBi_{25nm}$) required two cycles, while the 35 and 45 nm layers ($AgBi_{35nm}$ and $AgBi_{45nm}$) necessitated three cycles. After the lifting-off cycles, all the AgBi samples demonstrated nearly identical CV curves, indicating bismuth-selective redox behavior regardless of the initial Bi-layer thickness. Quantitative analyses of reduced Bi on the electrodes were performed by integrating the Bi reduction peaks in Fig. S7, where the reduced Bi quantity increased with Bi layer thickness (Fig. S8 and S9). For Bi layers thicker than 35 nm, the amount of Bi incorporated into the Ag nanoparticles reached a plateau, corresponding to the maximum electrochemically reducible Bi content.

The X-ray photoelectron spectroscopy (XPS) analysis revealed the oxidation states and atomic compositions of $AgBi_{15nm}$ and CV-$AgBi_{15nm}$ (Fig. 3 and Table S1). The Bi 4f spectra indicates that the surface of $AgBi_{15nm}$ is predominantly composed of Bi^{3+} species, such as Bi_2O_3. A minor metallic Bi component was also detected, which is attributed to the relatively thick Bi layer (15 nm) that likely protected the underlying regions from oxidation.

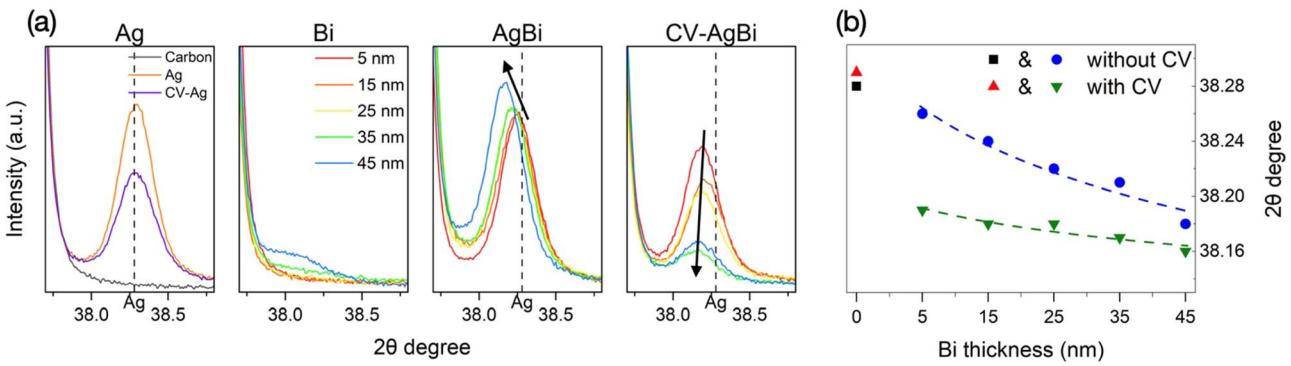

Fig. 4 XRD patterns of (a) carbon paper, Ag, Bi, AgBi, and CV-AgBi. (b) 2θ values of the Ag(111) diffraction peak (~38.2°). The peak at ~37.6° corresponds to the carbon paper (CP) substrate.

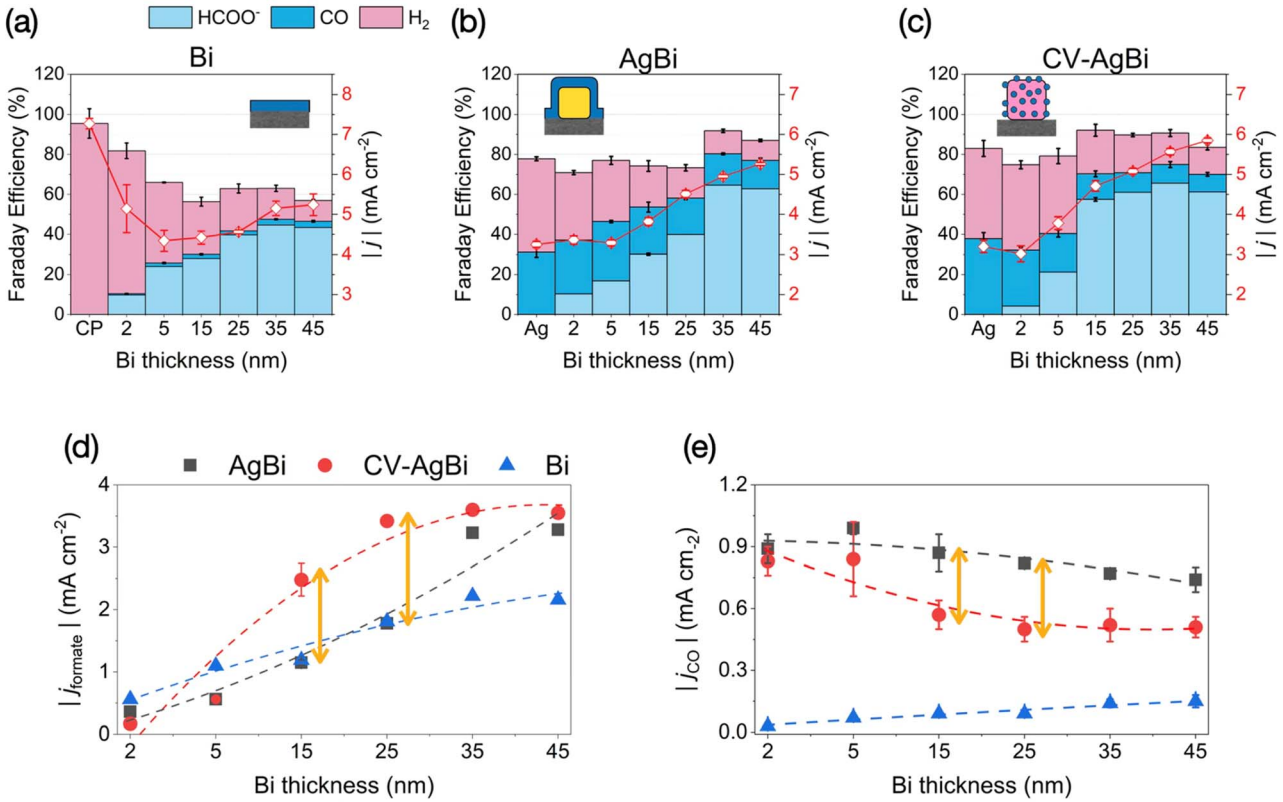

Fig. 5 Faradaic efficiencies and total current densities of (a) Bi, (b) AgBi, and (c) CV-AgBi electrodes. Partial current densities of each product for Bi, AgBi, and CV-AgBi: (d) formate ($j_{formate}$), (e) CO (j_{CO}).

The CV-$AgBi_{15nm}$ mostly has Bi^{3+} in the form of BiOCl[46] since the CV has been done in 0.1 M HCl solution. $AgBi_{15nm}$ showed exclusively metal state of Ag (Ag^0), whereas CV-$AgBi_{15nm}$ exhibited both Ag^0 and AgCl[47] components. The intensity of the Ag 3d peaks increased after CV, as the Bi overlayer was removed during the CV treatment. Notably, the chlorine to bismuth atomic ratio was approximately 4.7 (Fig. S10), far exceeding the 1 : 1 stoichiometry of BiOCl, corroborating the formation of an AgCl surface layer on Ag after CV.

The O 1s spectra also showed that $AgBi_{15nm}$ has lower binding energy of both non-defective (O1) and defective (O2) metal oxides,[48] consistent with the presence of Bi_2O_3, along with C–O bonds peak originating from oxygenated carbon electrode.[49] In contrast, CV-$AgBi_{15nm}$ exhibited the peaks with higher binding energy, assigned to C–O bonds and Nafion.[50] The absence of metal oxide related peaks (O1 and O2) in CV-$AgBi_{15nm}$ can be explained by the removal of most Bi species by CV, which exposed the underlying substrates. This interpretation was corroborated by the emergence of Nafion-related peaks in the C 1s (Fig. 3h) and S 2p (Fig. S10).[50]

Fig. S11 revealed that as the initial Bi thickness increases, the surface Bi concentration and the relative proportion of metallic Bi^0 significantly increase, with $AgBi_{35nm}$ sample exhibiting a complete shielding of the underlying Ag substrate as evidenced by the disappearance of Ag characteristic peaks.

This significant increase in metallic Bi^0 intensity at 35 nm is related to our XRD observations, which indicate a structural transition from a purely amorphous phase to a mixed amorphous–crystalline phase at this thickness. These findings directly support the electrochemical results, where $AgBi_{35nm}$ achieved higher formate yield and selectivity compared to samples with lower thickness.

While the Ag/AgCl ratio varies with CV cycling (Fig. S12), it appears to have a negligible direct impact on the steady-state activity since Ag/Cl is readily reduced to metallic Ag^0 during the initial stage of CO_2RR. The catalytic performance is primarily governed by the maximum density of active Bi single-atom species integrated within the reconstructed Ag matrix, which increases proportionally with the initial Bi loading.

The X-ray diffraction (XRD) patterns displayed the peaks corresponding to graphite ($2\theta \approx 37.6°$) and Ag(111) ($2\theta \approx 38.2°$) within the 2θ range of 37.5° to 39.0° (Fig. 4), while the peaks from other species were not observed in this region (Table S2). There was no noticeable peak shift of pure Ag before and after the CV process (Fig. 4a). Upon Bi deposition, the Ag(111) peak exhibited a clear shift toward lower angles compared to pure Ag, and the extent of this shift increased with increasing Bi layer thickness, confirming that bismuth atoms were diffused into the Ag lattice, resulting in the lattice expansion of Ag nanoparticles.[51–53] Furthermore, after the CV process, the Ag(111) peak of AgBi samples underwent an additional shift to lower angles, implying higher concentration of Bi in the Ag lattice through electrochemical treatments.

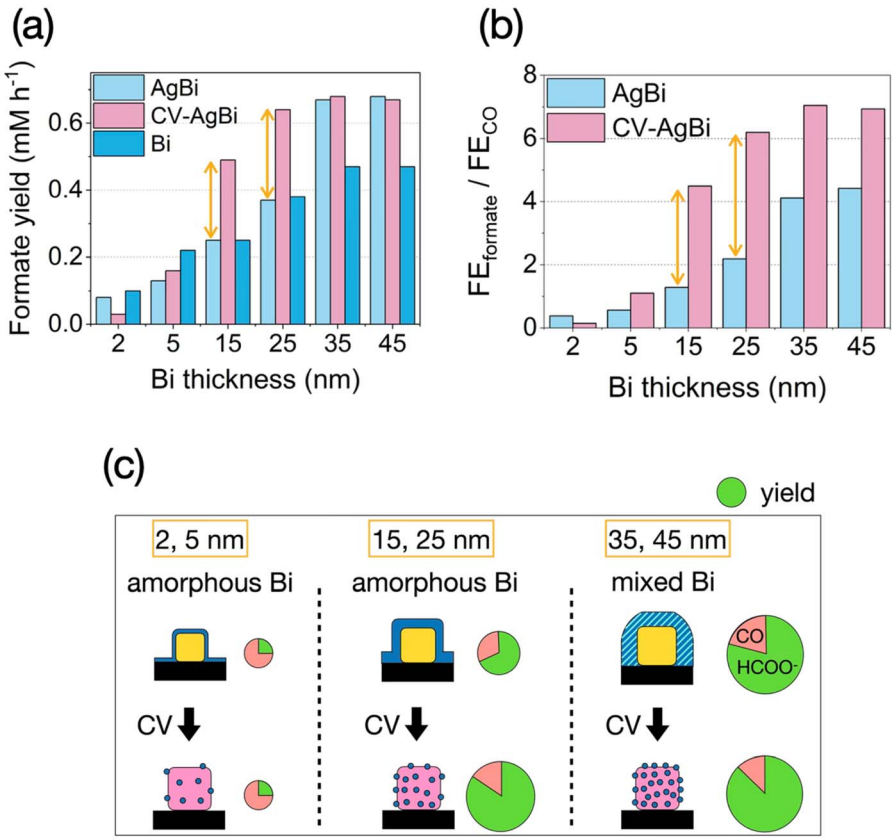

Fig. 6 Comparison of (a) formate yield and (b) faradaic efficiency ratio of formate/CO for AgBi and CV-AgBi as a function of Bi thickness, respectively. (c) Summary of catalytic performance change depending on Bi thickness.

Unlike the increasing shift of Ag(111) peaks in AgBi samples, the Ag(111) peaks of CV-AgBi samples gave the similar diffraction angles (38.16°–38.19°), regardless of the initial Bi thickness. Bi atoms diffuse into the Ag lattice up to approximately 2.3 weight percentage.[51] We expect that the Bi content in the AgBi samples reached an upper limit after the CV process, resulting in similar Ag(111) peak positions for CV-AgBi samples, regardless of the thickness of the initial Bi deposition.

The intensity of the Ag(111) peak decreased in the CV-treated samples, and this decrease was closely related to the number of CV cycles required to remove excess Bi. For instance, $AgBi_{5nm}$ requires 1 cycle; $AgBi_{15nm}$ and $AgBi_{25nm}$ required 2 cycles; and $AgBi_{35nm}$ and $AgBi_{45nm}$ required 3 cycles, as confirmed in Fig. S7. The variation of peak intensity is attributed to the partial transformation of surface Ag into AgCl by CV treatments in the HCl electrolyte. For Bi, the Bi(104) peak was absent in the AgBi samples with Bi thicknesses up to 25 nm, indicating that Bi predominantly existed as amorphous Bi_2O_3 under ambient conditions. Above 35 nm, a broad peak emerged and gradually increased in intensity with increasing thickness, indicating the formation of a metallic Bi phase.

The CV, TEM, XPS, and XRD analyses indicated that Bi single atoms on Ag nanoparticles were generated immediately after the CV treatment in 0.1 M HCl. During sample retrieval and washing, a thin BiOCl/AgCl passivation layer formed on the Ag surface, in which BiOCl existed as isolated species on AgCl (Fig. 1b–e). Upon applying a cathodic CO_2RR potential, AgCl and BiOCl were reduced to Ag[54] and Bi,[55,56] respectively. The resulting Bi atoms formed Bi–Ag SAAs rather than persistent Bi–O–Ag or Bi–Cl–Ag coordination. Consistent with the coordination-stability hierarchy (N > O ≫ Cl),[57–60] chloride coordination is far less robust than N- or lattice-O anchoring. Oxygen in robust oxide lattices can persist under cathodic bias,[56] whereas the oxygen associated with isolated BiOCl appeared only in trace amounts and was readily removed, thereby facilitating Bi–Ag coordination. Thus, CV treatment in HCl, followed by the application of a reducing potential, effectively removed Cl and O species and promoted Bi–Ag coordination, thereby facilitating the formation of Bi–Ag SAAs.

The electrochemical CO_2RR measurements were conducted under identical conditions (−1.5 V *vs.* Ag/AgCl (3 M KCl), CO_2-saturated 0.5 M $KHCO_3$ solution in H-cell) to investigate the influence of Bi single atoms on Ag *via* CV treatment (Fig. 5 and 6). As the Bi layer thickness increased in the Bi catalysts without Ag nanoparticles, both the FE and the partial current density for formate increased, whereas CO production showed only a modest rise to a thickness of 35 nm (Fig. 5a, d and e). As shown in Fig. 4a, Bi crystallinity increased with thickness, and Bi transformed into mixed amorphous–crystalline state. The mixed amorphous–crystalline Bi is reported to deliver higher formate production in CO_2RR than either purely amorphous or purely crystalline Bi.[61,62] Thus, CO_2RR performance shows the

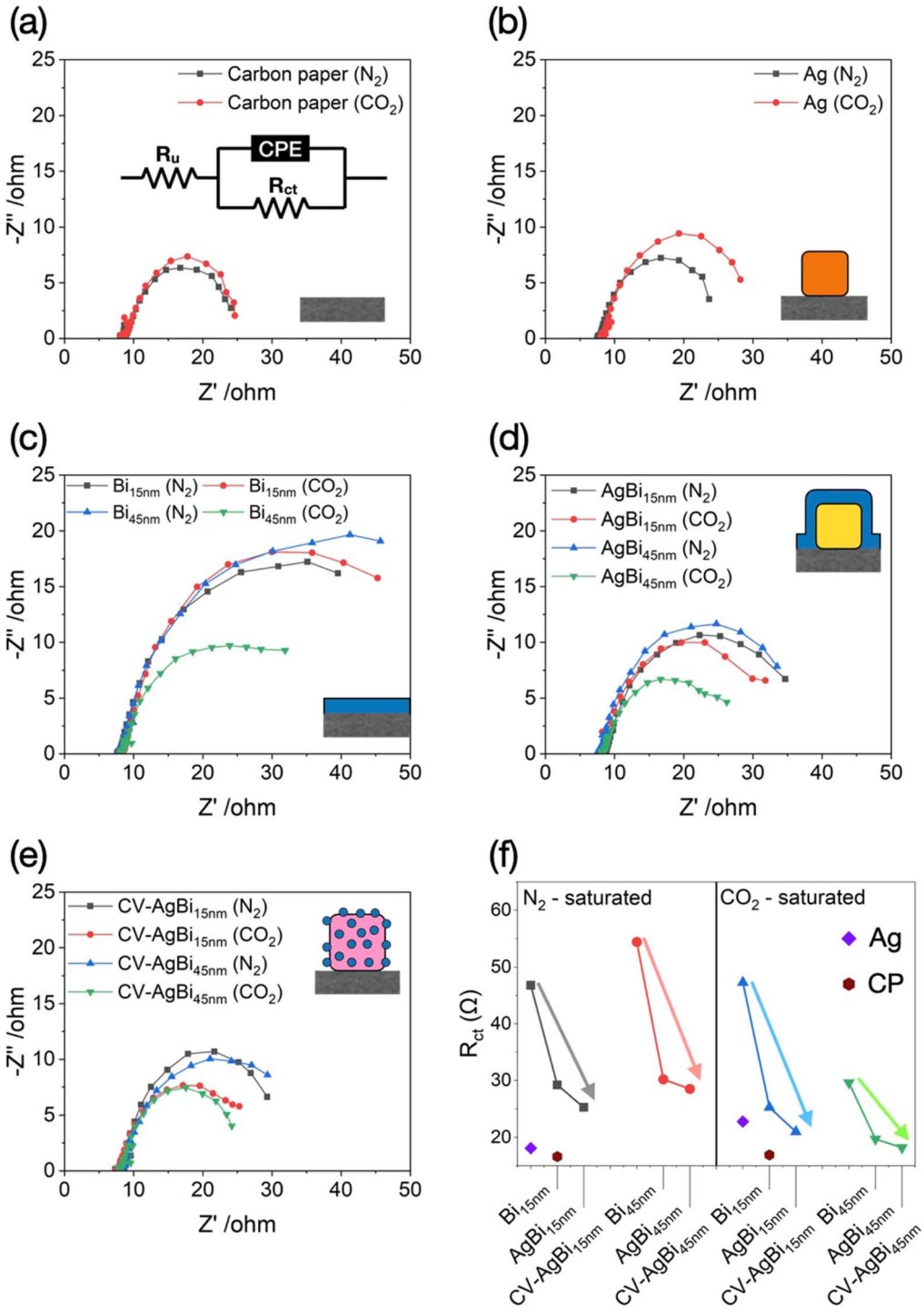

Fig. 7 Electrochemical impedance spectroscopy (EIS) Nyquist plots of (a) carbon paper, (b) Ag, (c) Bi_{15nm} and Bi_{45nm}, (d) $AgBi_{15nm}$ and $AgBi_{45nm}$, and (e) CV-$AgBi_{15nm}$ and CV-$AgBi_{45nm}$, measured in 0.5 M $KHCO_3$ under N_2- and CO_2-saturated conditions. (f) Comparison of charge transfer resistance (R_{ct}) values extracted from equivalent circuit fitting.

dependence on deposited Bi layer thickness. The formate yield reached a plateau because the extent of the amorphous–crystalline phase was similar for the 35 nm and 45 nm samples.

Meanwhile, both AgBi and CV-AgBi consistently exhibited higher FE_{CO} and j_{CO} values than Bi, which is attributable to the presence of Ag (Fig. 5b–e). Notably, AgBi showed ~1.5-fold higher j_{CO} values than CV-AgBi, even though the Ag surface was covered by a thick Bi overlayer. This suggests that the contribution of Ag to CO_2RR remains more pronounced in AgBi with a thick Bi coating than in CV-AgBi, where only Bi single atoms are present. Regarding formate production, both $FE_{formate}$ and $j_{formate}$ for AgBi and CV-AgBi exhibited a clear dependence on Bi layer thickness and exceeded those of Bi once the Bi thickness surpassed specific thresholds. In AgBi, $FE_{formate}$ and $j_{formate}$

became higher than those of Bi only when the Bi overlayer was thicker than 35 nm, whereas in CV-AgBi this transition occurred at a much lower thickness of 15 nm. This indicates that AgBi requires a substantially thicker Bi layer (35 nm) to suppress the catalytic influence of Ag and to enable formate formation by Bi. In contrast, CV-AgBi achieves comparable enhancement with only a 15 nm Bi layer, implying that Bi single atoms in CV-AgBi are intrinsically more efficient for formate production. The CO_2RR activity of the carbon electrode without metal catalysts and CV treated Bi 15 nm thickness samples showed only hydrogen evolution reaction (Fig. S13). The presence of Ag nanoparticles played a crucial role in the electrochemical reaction.

We assume that these results closely correlate with both the crystallinity of Bi and the amount of Bi incorporated into Ag. For AgBi samples with Bi layers thinner than 25 nm, the Bi phase is predominantly amorphous (Fig. 4a), which is known to yield relatively poor CO_2RR performance.[61,62] $j_{formate}$ for AgBi exceeds that of Bi only when the Bi thickness surpasses ~35 nm, where a mixed amorphous–crystalline phase forms and enhances activity. For CV-AgBi samples within the 15–25 nm range, sufficient Bi is reduced and anchored during CV to participate actively in CO_2RR (Fig. S8), producing a pronounced performance enhancement through synergistic effects with Ag. However, at very low thicknesses (2–5 nm), only a small amount of Bi is reduced during CV, leaving Ag to dominate the surface (Fig. S8), and thus the improvement after CV is negligible. Beyond 35 nm, the Bi layer existed in a mixed amorphous–crystalline phase, and the formate yield of Bi, AgBi, and CV-AgBi reached an upper limit (Fig. 6a). Notably, over 35 nm, the formate yield of thick Bi layer in AgBi was comparable to that of Bi single atoms in CV-AgBi, whereas the formate selectivity was substantially higher for CV-AgBi (Fig. 6b).

Depending on the Bi layer thickness, three distinct regimes were observed (Fig. 6c). For Bi layers of 2–5 nm, the CO_2RR performance was similar with and without CV treatment. For Bi layers of 15–25 nm, the CV process markedly enhanced formate production and selectivity, by factors of ~1.8 and ~3.2, respectively. For Bi layers of 35–45 nm, the catalysts exhibited comparable formate production regardless of CV treatment, whereas the formate selectivity increased by ~1.7-fold after CV.

Electrochemical impedance spectroscopy (EIS) analysis was conducted to evaluate charge transfer resistance (R_{ct}) under both N_2- and CO_2-saturated conditions (Fig. 7).[63] The bare carbon electrode exhibited identical R_{ct} values regardless of the gas environment (Fig. 7a), indicating that only HER occurred. Under N_2, Ag performed HER with a capability comparable to carbon paper, as evidenced by an R_{ct} only ~1.5 Ω higher (Fig. 7b). In contrast, under CO_2-saturated conditions, Ag showed a higher R_{ct} than under N_2, consistent with previous reports that the Nyquist semicircle reflects the charge-transfer process associated with CO_2RR.[63] Accordingly, the increased R_{ct} under CO_2 indicated the engagement of the CO_2 reduction pathway.

Under N_2-saturated conditions, AgBi samples exhibited lower R_{ct} values than pure Bi, and CV-AgBi samples showed an even further decrease in R_{ct} compared with AgBi (Fig. 7c–f). This result indicates that the Ag-modified Bi catalysts enable more facile charge transfer for CO_2RR. Under N_2-saturated conditions, the measured R_{ct} decreased in the order Bi > AgBi > CV-AgBi > Ag. The smaller R_{ct} under N_2 indicates that protons can participate more readily in the interfacial process, thereby facilitating hydrogen adsorption and evolution.[64] The interfacial charge transfer process in CO_2RR also involves protons or proton-containing reactants.[63,65] Enhanced dissociation of H_2O and HCO_3^- can facilitate the generation of sufficient protons and accelerate the hydrogenation of CO_2 to OCHO*, thereby improving the formate yield.[66] Based on the EIS results, we propose that AgBi and CV-AgBi enable more facile charge transfer to CO_2RR intermediates, as well as increased proton availability at the interface, thereby leading to higher rates of formate production. These electrochemical results demonstrated that the presence of Ag particles boosted formate formation relative to Bi-only samples, highlighting the superiority of the bimetallic configuration. Despite a substantially lower Bi loading, the single-atom configuration can deliver formate yields comparable to those of thick Bi, underscoring its maximized atom utilization of Bi in SAAs configuration.

4. Conclusion

We demonstrated a designed strategy for synthesizing Bi–Ag single-atom alloy catalysts (CV-AgBi) by converting a thermally evaporated Bi overlayer on Ag nanoparticles into atomically dispersed Bi species *via* cyclic voltammetry. Electrochemical measurements, together with structural and chemical analyses, confirmed the formation of atomically dispersed Bi, while EIS results indicate that Bi single atoms facilitate more efficient CO_2 activation through enhanced charge transfer and proton supply. Catalytically, the Bi single-atom configuration (CV-$AgBi_{15nm}$) increases the formate yield by 1.9-fold and boosts the formate selectivity ($FE_{formate}/FE_{CO}$) by 3.5-fold relative to the thick Bi overlayer ($AgBi_{15nm}$), despite requiring substantially less Bi. These findings highlight that cyclic voltammetry offers a simple and effective route for constructing Bi–Ag SAAs, and the concept is potentially extendable to other metal systems.

Author contributions

Yongsu An: conceptualization, methodology, formal analysis, investigation, visualization, writing – original draft. Sunglun Kwon: validation. Chan Woo Lee: writing – review and editing. Young Heon Kim: investigation, writing – review and editing. Duk-Young Jung: conceptualization, supervision, project administration, funding acquisition, writing – review and editing.

Conflicts of interest

The authors declare that they have no known competing financial interests or personal relationships that could have appeared to influence the work reported in this paper.

Data availability

Additional data supporting this article have been included as part of the supplementary information (SI). Numerical data can be made available upon request. Supplementary information is available. See DOI: https://doi.org/10.1039/d6ta00340k.

Acknowledgements

This research was supported by the Basic Research Lab (2022R1A4A1019296), by the National Research Foundation of Korea (RS-2025-25442528). S. Kwon acknowledges Sejong Science Fellowship Grants (RS-2024-00343195).

References

1 N. Sikdar, *Chem.–Eur. J.*, 2024, **30**, e202402477.
2 G. Leonzio, A. Hankin and N. Shah, *Chem. Eng. Res. Des.*, 2024, **208**, 934–955.
3 C. Xu, N. Wu, Y. Ran, P. Hong and Y. Lei, *Electrochem. Energy Rev.*, 2025, **8**, 35.
4 M. Grasemann and G. Laurenczy, *Energy Environ. Sci.*, 2012, **5**, 8171–8181.
5 A. Boddien and H. Junge, *Nat. Nanotechnol.*, 2011, **6**, 265–266.
6 F. Joó, *ChemSusChem*, 2008, **1**, 805–808.
7 J. F. Hull, Y. Himeda, W.-H. Wang, B. Hashiguchi, R. Periana, D. J. Szalda, J. T. Muckerman and E. Fujita, *Nat. Chem.*, 2012, **4**, 383–388.
8 Z. Yang, F. E. Oropeza and K. H. L. Zhang, *APL Mater.*, 2020, **8**, 060901.
9 P. Li, F. Yang, J. Li, Q. Zhu, J. W. Xu, X. J. Loh, K. Huang, W. Hu and J. Lu, *Adv. Energy Mater.*, 2023, **13**, 2301597.
10 S. Yang, M. Jiang, W. Zhang, Y. Hu, J. Liang, Y. Wang, Z. Tie and Z. Jin, *Adv. Funct. Mater.*, 2023, **33**, 2301984.
11 A. Husile, Z. Wang and J. Guan, *Chem. Sci.*, 2025, **16**, 5413–5446.
12 G. Wen, D. U. Lee, B. Ren, F. M. Hassan, G. Jiang, Z. P. Cano, J. Gostick, E. Croiset, Z. Bai, L. Yang and Z. Chen, *Adv. Energy Mater.*, 2018, **8**, 1802427.
13 W. Chen, Y. Wang, Y. Li and C. Li, *CCS Chem.*, 2023, **5**, 544–567.
14 H. Shen, T. Wang, H. Jiang, P. Zhao, Z. Chen, Y. Feng, Y. Cao, Y. Guo, Q. Zhang and H. Zhang, *Appl. Catal., B*, 2023, **339**, 123140.
15 Z. Xu, Z. Ao, M. Yang and S. Wang, *J. Hazard. Mater.*, 2022, **424**, 127427.
16 R. T. Hannagan, G. Giannakakis, M. Flytzani-Stephanopoulos and E. C. H. Sykes, *Chem. Rev.*, 2020, **120**, 12044–12088.
17 Q. Zhao, R. Gan, Y.-L. Ran, Q.-L. Ma, W.-W. Chen, Y.-X. Guo, Y. Zhang and D.-S. Wang, *Rare Met.*, 2024, **43**, 4903–4920.
18 S. Wang, L. Wang, D. Wang and Y. Li, *Energy Environ. Sci.*, 2023, **16**, 2759–2803.
19 Y. Da, R. Jiang, Z. Tian, X. Han, W. Chen and W. Hu, *SmartMat*, 2023, **4**, e1136.
20 J. Peng, L. Sun, Y. Li, Q. Zhang, X. Ren, X. Li, J. Zhang, X. Sun, Z. Song and L. Zhang, *Electrochem. Energy Rev.*, 2025, **8**, 16.
21 Y. An, Y. Lee, Y. Ji, Y. D. Kim, H. O. Seo and D.-Y. Jung, *Dalton Trans.*, 2024, **53**, 18346–18354.
22 X. Fan, W. Chen, L. Xie, X. Liu, Y. Ding, L. Zhang, M. Tang, Y. Liao, Q. Yang, X. Fu, S. Luo and J. Luo, *Adv. Mater.*, 2024, **36**, e2313179.
23 X. Xu, Y. Wei, L. Mi, G. Pan, Y. He, S. Cai, C. Zheng, Y. Jiang, B. Chen, L. Li, S. Zhong, J. Huang, W. Hu and Y. Yu, *Sci. China Mater.*, 2023, **66**, 3539–3546.
24 S.-Q. Liu, M.-R. Gao, S. Wu, R. Feng, Y. Wang, L. Cui, Y. Guo, X.-Z. Fu and J.-L. Luo, *Energy Environ. Sci.*, 2023, **16**, 5305–5314.
25 C. Xu, Y. Wang, W. Li, D. Gao, G. Wang and R. Cai, *ACS Appl. Mater. Interfaces*, 2024, **16**, 39305–39311.
26 H. Huang, Y. Wang, S. Zhang, Y.-C. Huang, Y.-R. Lu, C.-L. Chen, J. Ma, Z. Hu, J.-Q. Wang and L. Zhang, *ACS Nano*, 2025, **19**, 15509–15521.
27 Y. Jiang, J. Shan, P. Wang, L. Huang, Y. Zheng and S.-Z. Qiao, *ACS Catal.*, 2023, **13**, 3101–3108.
28 M. E. King, Y. Xu, P. Nagarajan, N. L. Mason, A. J. Branco, C. S. Sullivan, S. M. Silva, S. Jeong, F. Che and M. B. Ross, *Chem*, 2024, **10**, 1725–1740.
29 H. Jung, M. E. King and M. L. Personick, *Curr. Opin. Colloid Interface Sci.*, 2019, **40**, 104–117.
30 J. Hu, S. Zhou, Y. Sun, X. Fang and L. Wu, *Chem. Soc. Rev.*, 2012, **41**, 4356–4378.
31 C. Wang, W. Tian, Y. Ding, Y. Ma, Z. L. Wang, N. M. Markovic, V. R. Stamenkovic, H. Daimon and S. Sun, *J. Am. Chem. Soc.*, 2010, **132**, 6524–6529.
32 J. Zeng, C. Zhu, J. Tao, M. Jin, H. Zhang, Z. Li, Y. Zhu and Y. Xia, *Angew. Chem., Int. Ed.*, 2012, **51**, 2354–2358.
33 D. Bochicchio and R. Ferrando, *Phys. Rev. B: Condens. Matter Mater. Phys.*, 2013, **87**, 165435.
34 Q. Yin, F. Ma, Y. Zhou, Z.-J. Sui, X.-G. Zhou, D. Chen and Y.-A. Zhu, *J. Phys. Chem. C*, 2019, **123**, 18417–18424.
35 E. Puckrin and A. J. Slavin, *Phys. Rev. B: Condens. Matter Mater. Phys.*, 1990, **42**, 1168–1176.
36 M. Jia and J. T. Newberg, *Appl. Surf. Sci.*, 2021, **539**, 148219.
37 C. Wansorra, E. Bruder and W. Donner, *Acta Mater.*, 2020, **200**, 455–462.
38 C. Zhang, F. Liu, J.-J. Wang, G.-J. Wang, Z.-Y. Sun, Q. Chen, X.-P. Han, Y.-D. Deng and W.-B. Hu, *Microstructures*, 2025, **5**, 2025016.
39 S. E. Skrabalak, L. Au, X. Li and Y. Xia, *Nat. Protoc.*, 2007, **2**, 2182–2190.
40 Y. Wang, M. Wei, Q. Ding, H. Li and W. Ma, *Nano Lett.*, 2024, **24**, 4733–4740.
41 S. Wang, F. Li, J. Zhao, Y. Zeng, Y. Li, Z.-Y. Lin, T.-J. Lee, S. Liu, X. Ren, W. Wang, Y. Chen, S.-F. Hung, Y.-R. Lu, Y. Cui, X. Yang, X. Li, Y. Huang and B. Liu, *Nat. Commun.*, 2024, **15**, 10247.
42 P. Aich, H. Wei, B. Basan, A. J. Kropf, N. M. Schweitzer, C. L. Marshall, J. T. Miller and R. Meyer, *J. Phys. Chem. C*, 2015, **119**, 18140–18148.
43 W. Zhu, J. Y. Yang, X. H. Gao, J. Hou, S. Q. Bao and X. A. Fan, *Electrochim. Acta*, 2005, **50**, 5465–5472.

44 O. A. Oviedo, P. Vélez, V. A. Macagno and E. P. M. Leiva, *Surf. Sci.*, 2015, **631**, 23–34.
45 S. Hu, J. Yi, Y.-J. Zhang, K.-Q. Lin, B.-J. Liu, L. Chen, C. Zhan, Z.-C. Lei, J.-J. Sun, C. Zong, J.-F. Li and B. Ren, *Nat. Commun.*, 2020, **11**, 2518.
46 Z. Yang, D. Wang, Y. Zhang, Z. Feng, L. Liu and W. Wang, *ACS Appl. Mater. Interfaces*, 2020, **12**, 8604–8613.
47 X. Yao, X. Liu and X. Hu, *ChemCatChem*, 2014, **6**, 3409–3418.
48 C. Roiron, C. Wang, I. V. Zenyuk and P. Atanassov, *J. Phys. Chem. Lett.*, 2024, **15**, 11217–11223.
49 L. Zhang, L. Tu, Y. Liang, Q. Chen, Z. Li, C. Li, Z. Wang and W. Li, *RSC Adv.*, 2018, **8**, 42280–42291.
50 A. K. Friedman, W. Shi, Y. Losovyj, A. R. Siedle and L. A. Baker, *J. Electrochem. Soc.*, 2018, **165**, H733–H741.
51 I. Krastev, T. Valkova and A. Zielonka, *J. Appl. Electrochem.*, 2004, **34**, 79–85.
52 R. Añez, L. Cabral, E. Z. da Silva, E. Longo, J. Andrés and M. A. San-Miguel, *Comput. Mater. Sci.*, 2021, **197**, 110612.
53 I. Karakaya and W. T. Thompson, *J. Phase Equilib.*, 1993, **14**, 525–530.
54 X. Jin, J. Lu, P. Liu and H. Tong, *J. Electroanal. Chem.*, 2003, **542**, 85–96.
55 S. Subramanian, V. I. Chukwuike, M. A. Kulandainathan and R. C. Barik, *ChemElectroChem*, 2020, **7**, 2265–2273.
56 R. Pang, P. Tian, H. Jiang, M. Zhu, X. Su, Y. Wang, X. Yang, Y. Zhu, L. Song and C. Li, *Natl. Sci. Rev.*, 2020, **8**, nwaa187.
57 B. Qiao, A. Wang, X. Yang, L. F. Allard, Z. Jiang, Y. Cui, J. Liu, J. Li and T. Zhang, *Nat. Chem.*, 2011, **3**, 634–641.
58 T. Zhang, J. Jin, J. Chen, Y. Fang, X. Han, J. Chen, Y. Li, Y. Wang, J. Liu and L. Wang, *Nat. Commun.*, 2022, **13**, 6875.
59 Z. Zhang, C. Feng, C. Liu, M. Zuo, L. Qin, X. Yan, Y. Xing, H. Li, R. Si, S. Zhou and J. Zeng, *Nat. Commun.*, 2020, **11**, 1215.
60 L. Zhang, N. Jin, Y. Yang, X.-Y. Miao, H. Wang, J. Luo and L. Han, *Nano-Micro Lett.*, 2023, **15**, 228.
61 C. Qin, L. Xu, J. Zhang, J. Wang, J. He, D. Liu, J. Yang, J.-D. Xiao, X. Chen, H.-B. Li, Z. Yang and J. Wang, *ACS Appl. Mater. Interfaces*, 2023, **15**, 47016–47024.
62 Y. Wang, Z. Huang, Y. Lei, J. Wu, Y. Bai, X. Zhao, M. Liu, L. Zhan, S. Tang, X. Zhang, F. Luo and X. Xiong, *Chem. Commun.*, 2022, **58**, 3621–3624.
63 F. Bienen, D. Kopljar, S. Geiger, N. Wagner and K. A. Friedrich, *ACS Sustain. Chem. Eng.*, 2020, **8**, 5192–5199.
64 X. Guo, S.-M. Xu, H. Zhou, Y. Ren, R. Ge, M. Xu, L. Zheng, X. Kong, M. Shao, Z. Li and H. Duan, *ACS Catal.*, 2022, **12**, 10551–10559.
65 J. A. Intrator, D. A. Velazquez, S. Fan, E. Mastrobattista, C. Yu and S. C. Marinescu, *Chem. Sci.*, 2024, **15**, 6385–6396.
66 X. Li, C. Fang, R. Hu and J. Yu, *Chin. Chem. Lett.*, 2026, **37**, 111307.